Catalysis Today 180 (2012) 96–104

Contents lists available at ScienceDirect

Catalysis Today

journal homepage: www.elsevier.com/locate/cattod

Hydrogen production from ethanol steam reforming on $M/CeO_2/YSZ$ (M = Ru, Pd, Ag) nanocomposites

Ines A. Carbajal Ramos[a], Tiziano Montini[b], Barbara Lorenzut[b], Horacio Troiani[a], Fabiana C. Gennari[a], Mauro Graziani[b], Paolo Fornasiero[b,*]

[a] Centro Atómico Bariloche (CNEA) and Instituto Balseiro (UNCuyo), Consejo Nacional de Investigaciones Científicas y Técnicas (CONICET), (8400) S.C. de Bariloche, A. Bustillo km 9.5, Río Negro, Argentina

[b] Department of Chemical and Pharmaceutical Sciences, Center of Excellence for Nanostructured Materials, INSTM-Trieste Research Unit, CNR-ICCOM Trieste Research Unit, University of Trieste, Via L. Giorgieri 1, 34127 Trieste, Italy

ARTICLE INFO

Article history:
Received 20 December 2010
Received in revised form 9 March 2011
Accepted 19 March 2011
Available online 5 May 2011

Dedicated to Prof. Serafin Bernal, an exemplary scientific guide, in occasion of his retirement.

Keywords:
Ethanol steam reforming (ESR)
Hydrogen production
Nanostructured catalysts
Ceria based materials

ABSTRACT

$M/CeO_2/YSZ$ nanocomposites (M = Ru, Pd, Ag) were prepared by successive impregnation and tested in the ethanol steam reforming (ESR). $Ru/CeO_2/YSZ$ demonstrated good activity and stability under reaction conditions. $Pd/CeO_2/YSZ$ shows good initial activity but suffers of significant deactivation while the performances of the Ag-based sample were rather poor. A plethora of different structural (Powder XRD), microstructural (HR-TEM), morphological (surface area, CO chemisorption) and thermal analysis characterization techniques were used to evidence the modification of the samples induced by prolonged exposure to the reaction mixture. The promising performances of $Ru/CeO_2/YSZ$ were associated to the combination of the positive action of the metal selectivity to syn-gas and of CeO_2 in metal dispersion stabilization and coke deactivation prevention.

1. Introduction

In the last years, the research activities devoted to the development of new energy vectors or alternative fuels have rapidly increased due to the drivers for cleaner air and for reducing the dependence upon fossil fuels. In addition, the ever-growing world energy demand pushes for a diversification of energy sources with particular attention to renewables [1] and for the development of active and stable fuel cells (FC), able to guarantee high conversion efficiency [2]. Among the various options to meet global energy needs, hydrogen, in combination with FCs, is considered a very attractive energy vector. While, it is generally accepted that H_2 based fuel cells can contribute to preventing the environmental pollution generated by conventional combustion engines, many problems remain unsolved for its large scale use. These latter relate to the enormous cost for the necessary infrastructure, technological problems in sustainable hydrogen production, storage and distribution [3]. Nevertheless, the possibility to produce H_2 from a variety of resources by many different ways stimulates the research activities, with particular attention to the more sustainable options. At the present, steam reforming of natural gas and partial oxidation of coal or heavy hydrocarbons are the most commonly used and economically competitive methods for large scale hydrogen production [4]. There is a general consensus on the fact that any future energy scenario is based on a mix of energy sources with an increased contribution of the renewables ones. This applies also to hydrogen production, where its production from biomasses is a challenging task [3].

Many different raw materials and reactions have been proposed for hydrogen production [4–8]. Of these, great attention has been dedicated to ethanol conversion to syngas. In fact, large quantities of first generation ethanol are already produced by fermentation of sugars and more sustainable second generation ethanol can be obtained from lignocellulosics [9,10] Literature reports reveal that the ethanol conversion and selectivity to hydrogen strongly depend on the type of metal catalyst used, type of precursor, preparation methods, type of catalyst support, presence of additives, operating condition and temperature. Catalysts consisting of Rh and Ni loaded on different supports present so far the best activity and are the most commonly used for ethanol steam reforming (ESR) for hydrogen production [11–16]. During ethanol steam reforming, Rh supported on Al_2O_3, MgO or TiO_2 showed higher ethanol

* Corresponding author. Fax: +39 040 5583903.
E-mail address: pfornasiero@units.it (P. Fornasiero).

0920-5861/$ – see front matter © 2011 Elsevier B.V. All rights reserved.
doi:10.1016/j.cattod.2011.03.068

conversion and hydrogen production than Ru, Pt and Pd [17]. Pt promotes the Water Gas Shift Reaction (WGSR), but its activity in C–C bond rupture was found to be limited. The hydrogen production of Ru-based catalyst is comparable to that of Rh only at relatively high Ru loading (5 wt%). While promising stability was observed for Rh based systems, Ru induces dehydration of ethanol to form ethylene, leading to coke formation via polymerization. Therefore, suitable promoters/additives must be added to prevent coke formation for effective and stable operation [15]. In this scenario, ceria can play a major role. In fact, CeO_2-based materials are widely used in catalysis since they increase and stabilize the metal dispersion of noble metals [18,19] and are able to provide reactive lattice oxygen [20,21]. These latter factors increase the efficiency of oxidation reactions, such those involved in reforming processes, reducing the deposition of intermediates that, after polymerization and dehydrogenation, result in coke deposition and deactivation of the catalysts. Accordingly, CeO_2-based materials are largely present in Three-Way Catalysts [21,22], catalysts for reforming processes [23–31] (including ethanol steam reforming [14–16,32]) and for H_2 purification [33–36] and electrodes for Solid Oxide Fuel Cells (SOFCs). In the latter application, CeO_2 is used to (i) increase the rate of oxidation reaction, (ii) to avoid the undesired solid state reaction between Yttria-Stabilized Zirconia (YSZ – the most used electrolyte) and perovskitic materials used as electrode materials and (iii) to increase the length of the Triple Phase Boundary (TPB) [37–40]. Moreover, CeO_2-based materials are key components of anodes of SOFCs fed directly with liquid fuels, such as hydrocarbons [41–43] or alcohols (including ethanol) [44,45], operating internal reforming or direct oxidation of the fuel without the necessity of a preliminary reforming step to produce H_2.

In the present work, the activity of heterogeneous catalysts comprising Ru, Pd or Ag was evaluated with respect to H_2 production by ethanol steam reforming. The metals were deposited on a CeO_2/YSZ nanocomposite support in order to obtain a material with composition similar to that of SOFCs anodes.

2. Experimental

2.1. Catalyst preparation

CeO_2 (10 wt%)/YSZ support was prepared by impregnation of commercial Yttria Stabilized Zirconia (YSZ, Y_2O_3 7–9 mol%, Mel Chemicals) previously calcined at 750 °C for 24 h. Briefly, an appropriate amount of cerium ammonium nitrate ($(NH_4)_2Ce(NO_3)_6$, 99.9%, Aldrich) was dissolved in ethanol and YSZ was added under continuous stirring. After 2 h, the slurry was dried first at room temperature under reduced pressure for 6 h and then in air at 120 °C for 12 h. The material was calcined in a static oven at 600 °C for 5 h (heating rate 1 °C min^{-1}, cooling rate 4.5 °C min^{-1}).

Pd, Ru and Ag were supported on the CeO_2 (10%)/YSZ in order to obtain a nominal metal loading of 2 wt% by wet impregnation using aqueous solution of $Pd(NO_3)_3{\cdot}2H_2O$ (puriss. Fluka), $AgNO_3$ (puriss. Fluka) or $Ru(NO)(NO_3)_3$ (ChemPur). An appropriate amount of the metal precursor was dissolved in bidistilled water. After adding the CeO_2 (10%)/YSZ powder, the suspension was stirred for 2 h. The solvent was removed at reduced pressure and the solid dried at 120 °C overnight. Finally, the samples were calcined in a static oven at 400 °C for 5 (heating rate 1 °C min^{-1}, cooling rate 4.5 °C min^{-1}).

2.2. Characterization

CO chemisorption and BET surface area measurements were performed using a Micromeritics ASAP 2020 C analyzer. N_2 physisorption isotherms were collected at liquid nitrogen temperature on 0.1 g of sample, after evacuation at 350 °C overnight.

CO chemisorption experiments were performed at 35 °C. Previous to the chemisorption experiments, the calcined catalysts were subjected to a cleaning pretreatment at 500 °C for 1 h under O_2 (5%)/Ar flow followed by reduction at 150 °C in H_2 (5%)/Ar for 2 h and evacuation at 400 °C for 4 h. In order to avoid coke removal from aged samples, the cleaning pretreatment was not applied and only the reduction step was performed. Typically, 0.2 g of samples were used and an equilibration time of 10 min was employed. Adsorption isotherms were measured in the low pressure range (2–20 Torr) in order to minimize the CO adsorption due to carbonate formation on CeO_2. The so-called reversible adsorption was eliminated by the double isotherms method. A chemisorption stoichiometry CO:M = 1:1 and a spherical geometry were assumed for the metal nanoparticles.

Powder XRD patterns of the samples were recorded with a Philips PW 1710/01 diffractometer using Cu Kα radiation (λ = 0.154 nm). The data were collected with a 0.02° step size in the 2θ range from 10° to 100°, using a counting time of 10 s per point.

Temperature Programmed Reduction (TPR) experiments were performed using a Micromeritics AutoChem 2910 instrument on ~0.25 g of the calcined materials. The samples were cleaned at 350 °C for 1 h by pulsing of O_2 in an Ar flow every 75 s, then purged with Ar at 350 °C for 15 min and cooled to -70 °C. H_2 (5%)/Ar (40 mL min^{-1}) was admitted into the reactor and the flow allowed to stabilize for 30 min before increasing the temperature to 900 °C at 5 °C min^{-1}. H_2 uptake was monitored using a Thermal Conductivity Detector (TCD). After reduction, the flow was switched to Ar to remove adsorbed hydrogen and the temperature allowed to decrease to 427 °C. The reduced materials were re-oxidized by pulsing O_2 into the Ar flow at 427 °C until a stable area is obtained for the O_2 pulse (at least 40 pulses were injected into the flow).

ThermoGravimetric Analysis (TGA) were performed using a TA Instruments TGA Q500 instruments in flowing air (60 mL min^{-1}). Usually, 10 mg of the spent catalysts were loaded and water was desorbed in flowing air at 100 °C for 20 min, until a constant weight were obtained. After that, the temperature was increased up to 1000 °C with a heating rate of 10 °C min^{-1}.

High resolution-transmission electron microscopy studies were performed using a transmission electron microscopy (TEM Philips CM200 UT operating at 200 kV). Samples for TEM were prepared by dispersing a small amount of powder in hexane and depositing a drop of the resulting suspension on a commercial carbon coated copper grid.

2.3. Catalytic tests

Catalytic experiments were conducted in a U-shaped 4 mm ID quartz microreactor. Typically 32 mg of catalyst, diluted in a 1:2 weight ratio with high purity α-Al_2O_3 (Grace Davison, calcined at 1300 °C for 24 h), were used. EtOH/H_2O 1:5 mixture were injected into an Ar flow with a Hamilton Gastight syringe using an INSTECH Model 2000 syringe pump at a rate of 1.8 μL min^{-1}, in order to obtain an ethanol concentration of 1.0% by volume in the gas stream. All the transfer lines between syringe, reactor and GC were heated to 120 °C. Gas flow rates were ~32 mL min^{-1} to ensure GHSV values of ~60,000 mL g^{-1} h^{-1}.

Before testing the catalytic activity, the calcined materials were pretreated under O_2 (5%)/Ar at 350 °C for 1 h (40 mL min^{-1}, 10 °C min^{-1}) and activated by reduction in H_2 (5%)/Ar at 150 °C for 2 h (40 mL min^{-1}, 5 °C min^{-1}). The gaseous mixture was first introduced in the reactor at 150 °C for 1 h, before increasing the furnace temperature to 600 °C with a heating rate of 1 °C min^{-1}. After 2 h at 600 °C, the furnace was cooled to 150 °C at the same rate. The catalyst was subjected to two of these cycles before being tested isothermally at selected temperatures. Stability tests were

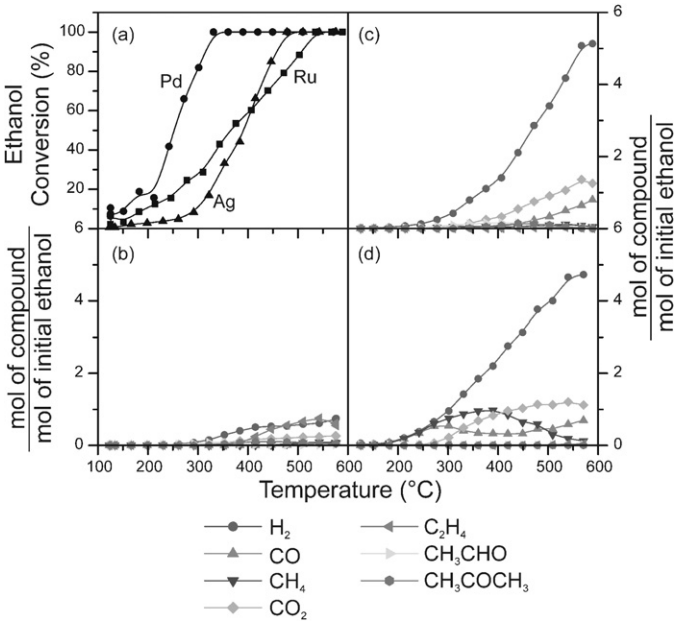

Fig. 1. Ethanol steam reforming activity on activated samples: overall ethanol conversion (a) and molar yields of products for $Ag/CeO_2/YSZ$ (b), $Ru/CeO_2/YSZ$ (c) and $Pd/CeO_2/YSZ$ (d). Conditions: EtOH (1.0%) + H_2O (5.0%) in Ar, GHSV ≈ 60,000 mL g^{-1} h^{-1}.

performed exposing the samples at the reaction mixture at 550 °C for at least 75 h.

On-line GC analysis was performed using a Hewlett Packard 5890 Series II gas chromatograph. A Molsieve 5A column, with Ar as carrier, was connected to a thermal conductivity detector (TCD) to analyze H_2, O_2, N_2, CH_4 and CO. A PoraPLOT Q column, with He as carrier, was connected in series to a methanator and to a flame ionization detector (FID) to analyze the carbon-containing compounds. C balance was always within ±2%.

3. Results and discussion

3.1. Catalytic activity under ESR

Fig. 1 shows the result of ethanol steam reforming on the $M/CeO_2/YSZ$ nanocomposites. The contribution of the homogeneous reaction (evaluated with an empty reactor) is negligible while blank experiments performed using α-Al_2O_3 alone (the diluent of the catalysts) evidences only the formation of ethylene at high temperature (above 500 °C) with a maximum ethanol conversion of ~18% at 600 °C.

Ethanol conversion starts around 150 °C, independently of the investigated catalyst (Fig. 1a). Significant differences in the hydrogen yields and selectivity are however observed with temperature depending on the nature of the metal phase.

$Ag/CeO_2/YSZ$ (Fig. 1b) shows poor activity in ethanol steam reforming: the main products are H_2 and acetaldehyde in all the temperature range investigated (yield up to 0.8 mol_{H_2} mol_{EtOH}^{-1}) while only minor amounts of CO_2 are produced above 400 °C.

$Ru/CeO_2/YSZ$ (Fig. 1c) shows a progressive increase in the ethanol conversion up to 550 °C. At the same time, H_2 production continuously increases reaching a maximum of 5.2 mol_{H_2} mol_{EtOH}^{-1} at 580 °C. Between 200 and 500 °C, H_2 and CO_2 production is accompanied with the production of low amounts of by-products, such as acetaldehyde, acetone and methane (molar yields always below 10 mol%). CO production is significant only above 450 °C. Above 500 °C, when ethanol conversion is total, only H_2, CO and CO_2 are detected in the gas phase, with a relative ratio in good agreement with the WGSR equilibrium.

$Pd/CeO_2/YSZ$ (Fig. 1d) converts completely ethanol above 350 °C and H_2 production reaches the maximum of 4.8 mol_{H_2} mol_{EtOH}^{-1} at 580 °C. At intermediate temperatures, the selectivity in the various by-products is very different with respect to the $Ru/CeO_2/YSZ$ sample. In fact, very large quantities of CH_4 are produced between 200 and 580 °C while acetaldehyde, acetone and ethylene are observed only in very minor amounts (molar yields below 5%).

The differences in the activity observed for the various samples can be discussed considering the reaction network proposed for the ethanol steam reforming [16]. The most favorable pathway involves the dehydrogenation of ethanol to acetaldehyde, that can be subsequently decomposed to CH_4 and CO. Then, CH_4 must be subjected to steam reforming, obtaining a mixture of H_2, CO and CO_2, depending from the WGSR equilibrium [16]. Acetone is obtained by a side reaction involving a condensation, oxidation and decarboxylation and is promoted by CeO_2-based materials and basic oxides [46]. On the other hand, dehydration of ethanol results in ethylene production. Subsequently, ethylene can be subjected to steam reforming producing H_2, CO and CO_2, depending once again from the WGSR equilibrium [16]. Dehydrogenation reactions require the use of a metal catalyst to activate the C–H and O–H bonds [47,48] while dehydration to ethylene is usually promoted by the acid sites of the oxide support [13]. Ru and Pd demonstrates a good activity in the activation of C–H and O–H bonds and, in agreement with this fact, many studies report their use as active phases for reforming of hydrocarbons [49–51] or oxygenates [50,52,53]. The differences in selectivity between Ru and Pd could be interpreted with a different catalytic behavior during acetaldehyde decomposition, suggesting the possibility of a new step in the reaction mechanism. Pd follows the pathway usually reported for ethanol steam reforming: acetaldehyde is decomposed to an equimolar mixture of CH_4 and CO, followed by steam reforming of methane and WGSR. On $Ru/CeO_2/YSZ$ only minor amounts of CH_4 were detected in the medium temperature range, although H_2, CO and CO_2 amounts continuously increased with increasing temperature. This could be an indication that CH_4 is easily reformed on the Ru-based catalyst or CH_4 is not formed by acetaldehyde decomposition. Usually, quite low conversions are observed in this temperature range (300–500 °C) on Ru-based catalysts during methane reforming processes [54–56]. Therefore, it is reasonable that CH_4 is formed only in limited amounts during ethanol steam reforming and that the reaction proceeds through decomposition of acetaldehyde to CH_3 and CHO groups adsorbed on the metal surface, where they are easily reformed to finally obtain syn-gas (H_2, CO and CO_2). On the other hand, $Ag/CeO_2/YSZ$ is the less active in ethanol reforming due to the inability of Ag to dissociate C–H bonds of hydrocarbons [57]. Since it does not react on the metal surface, ethanol is available for the reaction of the acid sites of the support producing ethylene as major product.

Prolonged stability tests were performed only on Ru- and Pd-based catalysts, since they demonstrate promising performances under ethanol steam reforming. Fig. 2 presents the results obtained during stability tests performed for 75 h at 550 °C. In both the cases, initial conversion and selectivity in the different products (H_2, CO, CO_2 and CH_4) are in excellent agreement with the values obtained at the same temperature during run-up experiments. No significant deactivation of the catalytic performances is observed during the overall experiment for $Ru/CeO_2/YSZ$ (Fig. 2a). On the other hand, $Pd/CeO_2/YSZ$ shows, after an initial period of 40 h of stable performance, a progressive decrease of ethanol conversion. At the same time, a progressive decrease in the molar yields of H_2, CO, CO_2 and CH_4 was observed.

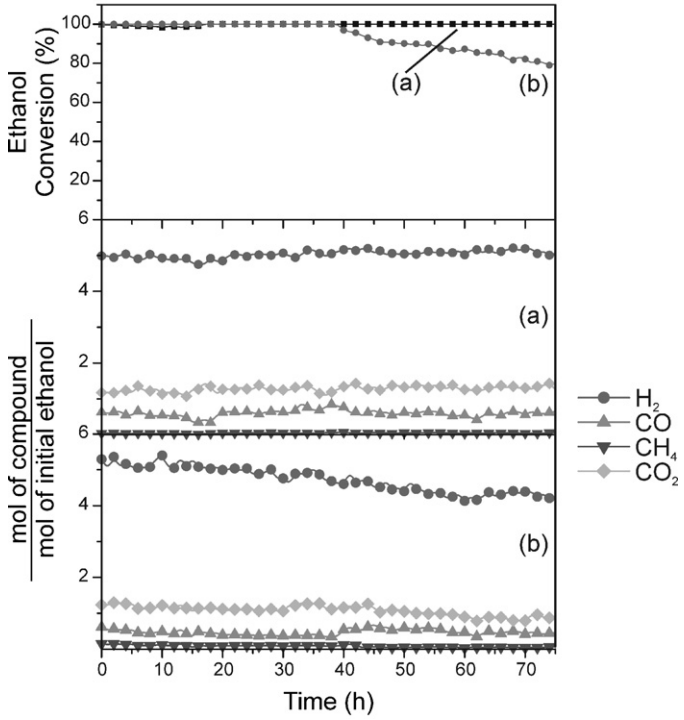

Fig. 2. Stability of ethanol steam reforming activity on activated samples: overall ethanol conversion (upper panel) and molar yields of products (central and lower panel) for $Ru/CeO_2/YSZ$ (a) and $Pd/CeO_2/YSZ$ (b). Conditions: EtOH (1.0%) + H_2O (5.0%) in Ar, GHSV ≈ 60,000 mL g^{-1} h^{-1}, T = 550 °C.

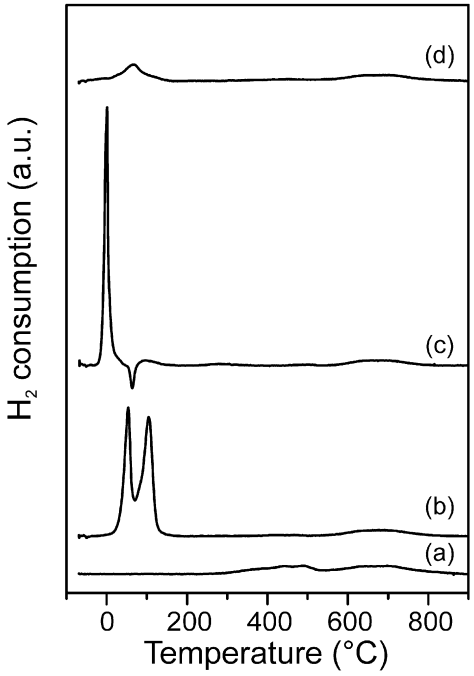

Fig. 3. Temperature Programmed Reduction (TPR) profiles for CeO_2/YSZ (a), $Ru/CeO_2/YSZ$ (b), $Pd/CeO_2/YSZ$ (c) and $Ag/CeO_2/YSZ$ (d).

3.2. Characterization of $M/CeO_2/YSZ$ nanocomposites (M = Ru, Pd, Ag)

3.2.1. Temperature Programmed Reduction (TPR)

Temperature Programmed Reduction (TPR) experiments were performed to assess the reducibility of the materials and to select the best conditions for the activation of the catalysts before catalytic experiments (complete reduction of the metal phases). TPR were performed from −70 °C in order to gain information on the low temperature reduction of palladium oxide and on its hydrides formation.

CeO_2/YSZ support shows the typical TPR profile of supported CeO_2 (Fig. 3a). Two broad reduction peaks are observed. The first one (250–550 °C) is the convolution of various reduction processes. This TPR peak can be ascribed to the reduction of the surface of CeO_2 particles and/or to the reduction of highly dispersed CeO_2 nanocrystals [58,59]. The second peak (550–900 °C) is ascribed to the reduction of the bulk of CeO_2 particles [60].

The presence of a easily reducible metal oxide (ruthenium, palladium or silver oxide) significantly promotes the reduction of surface ceria/small ceria nanoparticles [61]. Vice versa, the reduction of bulk ceria–high temperature peak–is not significantly affected by the presence of supported metals. The H_2 consumption at low temperature corresponds to the contribution of both the reduction of supported metal oxide and of the surface of ceria. The values significantly differ among the samples due to the different composition of the metal oxides present after impregnation (RuO_2, PdO and Ag_2O, see below, XRD section). $Ru/CeO_2/YSZ$ (Fig. 3b) presents two sharp reduction peaks centered at 50 and 105 °C. $Pd/CeO_2/YSZ$ (Fig. 3c) shows a very sharp and intense H_2 consumption with maximum at 0 °C, followed by a negative peak centered at 65 °C ascribed to the decomposition of PdH_x species. Finally, $Ag/CeO_2/YSZ$ (Fig. 3d) presents a broad reduction peak centered around 70 °C. Despite the different behavior in the low temperature range, the reduction processes are completed at 150 °C for all the impregnated samples. Therefore, this temperature was selected for the activation of the catalysts before each catalytic activity experiments.

After reduction, the amount of reduced species was evaluated by O_2 pulses at 427 °C, as a generally accepted procedure reported in the literature [20]. An O_2 consumption of 112 μmol O_2 g^{-1} was measured for CeO_2/YSZ. Assuming that only cerium is involved in the redox process at these temperature, the data indicate that ~77% of the cerium is reduced to Ce(III). This value is significantly higher than usually obtained for bulk CeO_2 [20]. This discrepancy could be related with the high interaction between CeO_2 and YSZ. In fact, Kim et al. reported that CeO_2 impregnated on YSZ remains reduced at higher $p(O_2)$ compared to pure CeO_2 [59]. Moreover, Putna et al. reported that CeO_2 films on YSZ are much easily reducible with respect to CeO_2 films of α-Al_2O_3, as a result of the structure-directing properties of zirconia surfaces which induce a high concentration of defects in CeO_2 overlayers [62]. For $Ag/CeO_2/YSZ$, an O_2 consumption close to that of CeO_2/YSZ is obtained (109 μmol O_2 g^{-1}), suggesting that the re-oxidation of Ag is minimal under these conditions (high temperature pre-reduction, that leads to metal sintering and low temperature oxidation). On the other hand, for $Ru/CeO_2/YSZ$ and $Pd/CeO_2/YSZ$ the O_2 consumption is much higher, 204 and 168 μmol O_2 g^{-1} respectively. Assuming that the same O_2 consumption from reduced CeO_2, the difference can be related with the oxidation of the metal phases. Taking this into account, a molar O/M ratio of 0.46 and 0.30 can be calculated for Ru- and Pd-based samples, respectively. This is an indication that, after the severe sinterization expected for the metals after the TPR, their full re-oxidation is not possible and O_2 consumption results mainly in the passivation of the metal surface or in the formation of an oxide layer on the surface of large metal cores.

3.2.2. N_2 physisorption

N_2 physisorption at the liquid nitrogen temperature was employed to investigate the evolution of the textural properties of the samples from their preparation to the end of the catalytic activity experiments. YSZ support calcined at 750 °C for 24 h presents a

Table 1
N_2 physisorption results for $M/CeO_2/YSZ$ (M = Ru, Pd, Ag) after various treatments.

Sample	SSA[a] ($m^2\,g^{-1}$)	CPV[b] ($mL\,g^{-1}$)	d_M[c] (nm)
Calcined			
YSZ	47	0.17	11/27
CeO_2/YSZ	41	0.15	10/40
$Ru/CeO_2/YSZ$	42	0.15	10/28
$Pd/CeO_2/YSZ$	42	0.15	10/28
$Ag/CeO_2/YSZ$	41	0.13	10/28
Activated/reduced			
$Ru/CeO_2/YSZ$	37	0.15	10/28
$Pd/CeO_2/YSZ$	39	0.13	10/27
$Ag/CeO_2/YSZ$	40	0.16	11/38
Run-up			
$Ru/CeO_2/YSZ$	39	0.16	10/55
$Pd/CeO_2/YSZ$	38	0.14	10/28
$Ag/CeO_2/YSZ$	40	0.16	10/55
After stability test			
$Ru/CeO_2/YSZ$	38	0.16	10/38
$Pd/CeO_2/YSZ$	32	0.12	10/28
After regeneration[d]			
$Ru/CeO_2/YSZ$	39	0.15	10/39
$Pd/CeO_2/YSZ$	36	0.14	10/38

[a] Specific Surface Area from BET analysis.
[b] Cumulative Pore Volume determined from the desorption branch of physisorption isotherms.
[c] Relative maxima of the pore distribution determined by the BJH analysis from the desorption branch of the physisorption isotherms.
[d] After stability tests, the catalysts were cleaned by oxidative treatment at 500 °C for 1 h to remove carbonaceous deposits e reduced in H_2/Ar at 150 °C for 1 h.

physisorption isotherm typical of a mesoporous material with a bimodal distribution of the pores, with relative maxima centered around 10 and 30 nm. The impregnation with CeO_2 produces a slightly decrease of the surface area and pore volume while the subsequent impregnation with the metal precursors do not further modify the texture on the materials. (Table 1) The textural properties of the samples are marginally affected by the activation by H_2 reduction at 150 °C and after two consecutive run-up experiments up to 600 °C under ESR condition. A significant decrease in the surface area and pore volume is observed only for the $Pd/CeO_2/YSZ$ sample after stability tests. Finally, an oxidative treatment at 500 °C performed on the spent $Pd/CeO_2/YSZ$ catalyst results in a partial recovery of the initial surface area and pore volume. These results suggest that the deposition of carbonaceous compounds on the surface of the $Pd/CeO_2/YSZ$ catalyst significantly contributes to the deactivation process resulting in a partial pore blocking. Remarkably, the textural properties $Ru/CeO_2/YSZ$ are almost unaffected by the prolonged exposure under ESR conditions at 550 °C, suggesting that the coke deposition takes place in a lower extent with respect to $Pd/CeO_2/YSZ$ and does not significantly affect the activity performance.

3.2.3. Powder X-ray diffraction

Powder XRD patterns were collected on the samples after activation (H_2 reduction at 150 °C) and after aging under ESR condition (both after run-up experiments and stability tests). The XRD patterns are dominated by the reflection of tetragonal YSZ (space group $P4_2/nmc$) and cubic CeO_2 (space group Fm3 m). Notably, after calcination at 400 °C, very weak and broad reflections of metal oxide phases are observed (data not shown), indicating the presence of RuO_2, PdO and Ag_2O in the samples. After activation by reduction at 150 °C (Fig. 4), very weak reflections related to metal phases can be observed. Their intensity significantly increases after aging under ESR conditions, suggesting a partial sintering of the metal nanoparticles (Fig. 5). Rietveld analysis of the XRD patterns allows to estimate the weight percentages and the cell parameters of each component in the nanocomposite catalysts. Notably, Rietveld analysis can underestimate the amount of metal active phase, especially

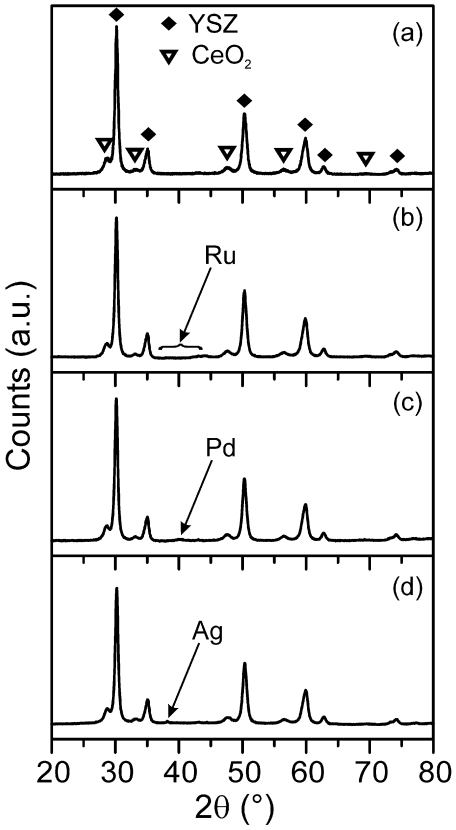

Fig. 4. Powder XRD patterns of CeO_2/YSZ (a), $Ru/CeO_2/YSZ$ (b), $Pd/CeO_2/YSZ$ (c) and $Ag/CeO_2/YSZ$ (d) after activation by H_2 reduction at 150 °C for 2 h.

when metal nanoparticles are highly dispersed on medium–high surface area supports. In the present study, the amount of each phase, determined from Rietveld analysis, is very close to the nominal values (2 wt% for the metals, 10 wt% for CeO_2, 88 wt% for YSZ) for all the samples treated at high temperatures (after two run-up experiments at 600 °C or after prolonged aging at 550 °C). This suggests that the XRD data can provide a representative description of those samples. On the other hand, after activation by reduction at 150 °C, the amount of metal estimated by Rietveld analysis is significant lower with respect to the nominal value (about 1 wt% in all the cases), suggesting that part of the metal is present in a very dispersed form on the surface of the catalysts and hardly detected by XRD. The cell parameters are in good agreement with the theoretical values. Moreover, they are not influenced in a significant extent by the thermal/chemical treatments subjected by the samples. Notably, this fact indicates that no solid state reaction between the components (in particular, CeO_2 and YSZ) takes place, as a result of cation diffusion during prolonged high temperature treatment.

Table 2 summarizes the mean crystallite sizes obtained for the different phases. The mean crystallite sizes of YSZ and CeO_2 are not affected by the various treatments of the materials. Since the intensities of the reflections of the oxides of the metals impregnated on the CeO_2/YSZ support are very low, their crystallite sizes cannot be calculate. On the other hand, the mean crystallite sizes of the metal phases significantly increases during tests under ESR conditions with respect to the correspondent values after activation (H_2 reduction treatment), indicating a partial sintering of the metal nanoparticles during ethanol reforming.

3.2.4. CO chemisorption

CO chemisorption was employed to evaluate the accessibility of the metal phases. Generally speaking, the selection of the

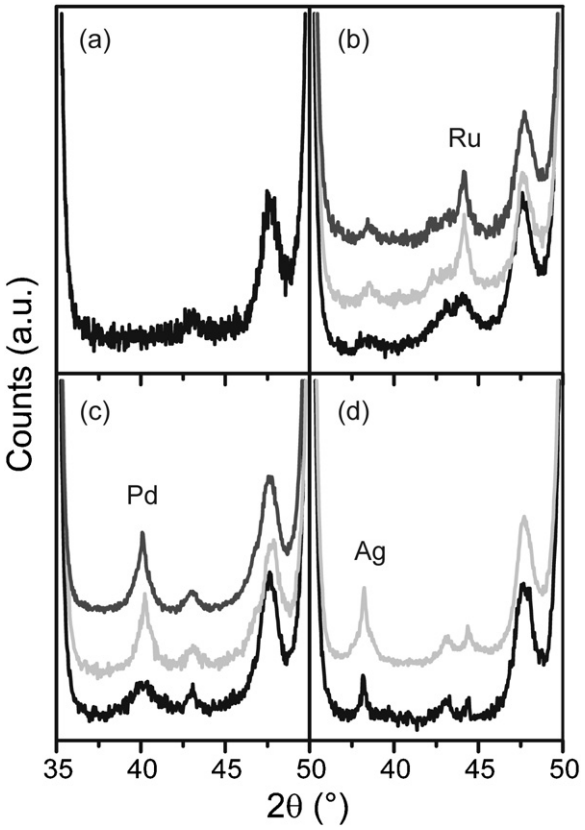

Fig. 5. Detail of the powder XRD patterns in the range 32–50° for CeO_2/YSZ (a), Ru/CeO_2/YSZ (b), Pd/CeO_2/YSZ (c) and Ag/CeO_2/YSZ (d) after activation by H_2 reduction at 150 °C for 2 h (black lines), after two consecutive run-up experiments under ESR conditions to 600 °C (light grey lines) and after stability tests under ESR conditions at 550 °C for 75 h (dark grey lines).

experimental conditions is crucial to obtain a reliable estimation of the fraction of atoms exposed to the gas phase. In particular, significant experimental problems can be encountered for the determination of the metal dispersion of CeO_2-based materials. In fact, hydrogen spillover from the metal to the support could take place during the chemisorption, resulting in a significantly high gas

Table 2
Mean crystallite sizes calculated for the phases present in M/CeO_2/YSZ (M = Ru, Pd, Ag) after various treatments.

Sample	Mean crystallite size[a] (nm)		
	YSZ	CeO_2	Metal
Calcined			
CeO_2/YSZ	17	10	–
Ru/CeO_2/YSZ	18	10	N.C.[b]
Pd/CeO_2/YSZ	18	10	N.C.[b]
Ag/CeO_2/YSZ	17	9	N.C.[b]
Activated/Reduced			
Ru/CeO_2/YSZ	17	10	9
Pd/CeO_2/YSZ	17	10	9
Ag/CeO_2/YSZ	17	10	10
After run-up experiments			
Ru/CeO_2/YSZ	17	10	16
Pd/CeO_2/YSZ	17	9	12
Ag/CeO_2/YSZ	17	9	16
After stability test			
Ru/CeO_2/YSZ	17	8	19
Pd/CeO_2/YSZ	17	8	13

[a] Determined applying the Scherrer's formula to the main reflection of each phase.
[b] Not calculated: the intensities of reflections from oxide phases related to the metals impregnated on the supports are too low for a reliable estimation of the crystallite sizes.

Table 3
CO chemisorption results for M/CeO_2/YSZ (M = Ru, Pd) after various treatments.

Sample	CO chemisorption		
	CO/M[a]	Apparent particle size[b] (nm)	Metal surface area[b] ($m^2\ g^{-1}$)
Activated/reduced			
Ru/CeO_2/YSZ	0.360	3.7	2.63
Pd/CeO_2/YSZ	0.093	12.0	0.83
After stability test			
Ru/CeO_2/YSZ	0.195	6.8	1.43
Pd/CeO_2/YSZ	0.006	190	0.05
After regeneration[c]			
Ru/CeO_2/YSZ	0.246	5.4	1.80
Pd/CeO_2/YSZ	0.079	14.2	0.70

[a] Assuming a CO/M stoichiometry of 1.
[b] Calculated assuming a spherical geometry of the metal particles
[c] After stability tests, the catalysts were cleaned by oxidative treatment at 500 °C for 1 h to remove carbonaceous deposits e reduced in H_2/Ar at 150 °C for 1 h.

consumption during the experiments [63]. In addition, presence of reduced ceria can lead to suppression of chemisorptions capability [63,64]. Hydrogen spillover effects can be limited by reducing the chemisorption temperature or with a careful selection of the partial pressure of the probe gas [64,65]. However, in the case of Pd–ceria based materials, the low temperature chemisorption cannot be applied due to the formation of PdH_x species with different stoichiometry depending from the H_2 pressure and the dimension of the metal nanoparticles. Furthermore, the kinetic of H_2 adsorption on Ru is very low at room temperature and chemisorption experiments must be performed at high temperature, where unfortunately spillover is maximized. Therefore, CO chemisorption appears as the best option to simultaneously investigate the accessibility of both Ru- and Pd-based samples. Chemisorption experiments were conducted in a low pressure range (1–20 Torr) to minimize the formation of carbonates on the CeO_2 support.

Ru/CeO_2/YSZ presents a higher metal accessibility with respect to Pd/CeO_2/YSZ (Table 3). This could be due to a different dispersion of the metal or to a different sensitivity of the two metals with respect to the electronic deactivation by reduced CeO_2, being Pd more sensitive than Ru. Notably, this latter deactivation is usually observed after more severe reductive treatment than those involved in activation of the catalysts (150 °C). The occurrence of electronic deactivation cannot be excluded in the case of the samples after stability tests, exposed to the reductive environment at 550 °C for prolonged time.

The apparent Ru particle size estimated from chemisorption (Table 3), is lower with respect to the mean crystallite size determined by XRD (Table 2), suggesting the presence of a considerable fraction of highly dispersed Ru nanoparticles. In fact, XRD broadening overestimates the mean crystallite dimensions when a relevant fraction of highly dispersed metal nanoparticles are present: the reflection intensity is mainly due to large, ordered particles while the very small, disordered metal particles scarcely contribute to diffraction of X-rays. On the other hand, a best agreement is observed in the case of Pd. After stability test under ESR conditions at 550 °C for 75 h, the accessible surface area is strongly reduced for both the catalysts investigated, as a result of coke deposition (see below), sintering, possible electronic deactivation or, but unlikely, occurrence of metal particle decoration (no evidence by TEM, see below). The accessibility of the metal is recovered after oxidative treatment at 500 °C, that removes carbon deposits and re-oxidize CeO_2.

3.2.5. High resolution Transmission Electron Microscopy (HR-TEM)

Transmission Electron Microscopy (TEM) was employed to investigate the morphology of the samples and their possible mod-

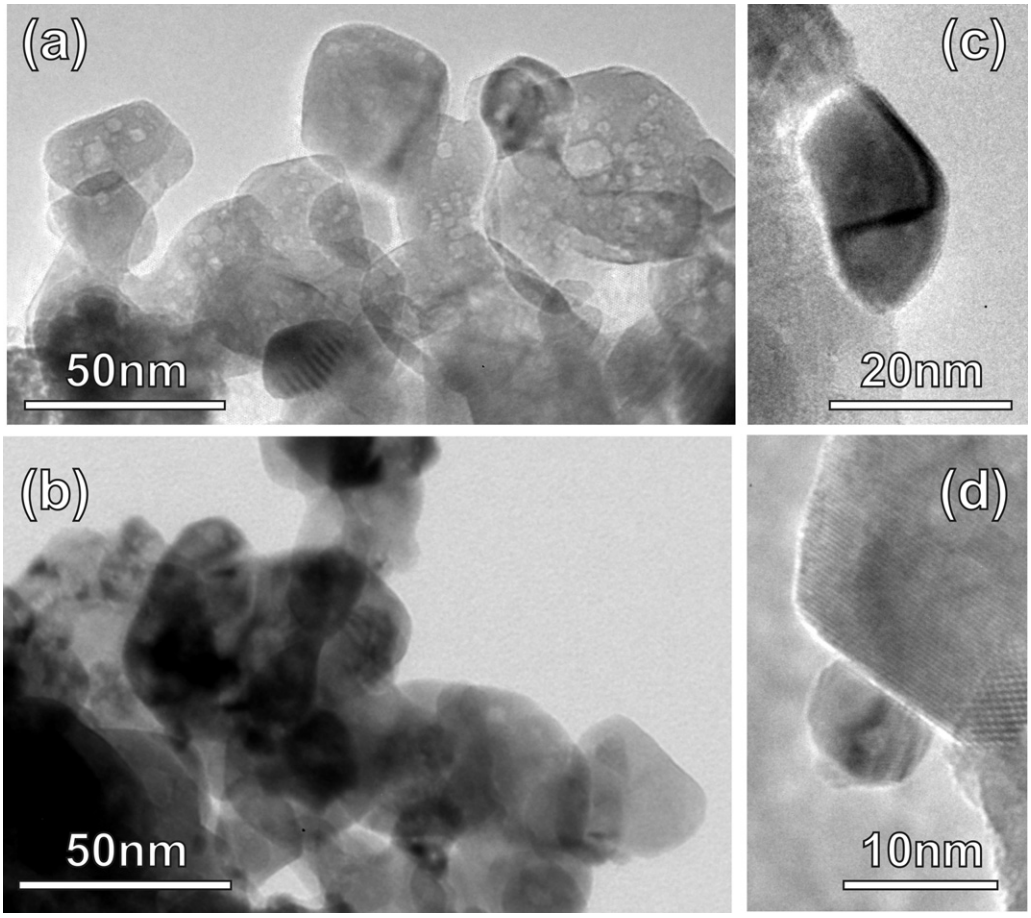

Fig. 6. TEM images of samples after activation by H_2 reduction at 150 °C for 2 h for Ru/CeO_2/YSZ (a) and Pd/CeO_2/YSZ (b) and representative HR-TEM images of metal nanoparticles for Ru/CeO_2/YSZ (c) and Pd/CeO_2/YSZ (d).

ifications after working under ESR conditions. TEM investigation of the YSZ and CeO_2/YSZ supports (data not shown) allow to evidence their morphology, helping in the identification of metal particles in the reduced samples. YSZ is composed by round-shaped, large grains (15–20 nm), strongly interconnected within each other. CeO_2 particles deposited on the YSZ support can be recognized as smaller, shaped particles with dimensions of 5–10 nm, that are uniformly distributed on the YSZ grains. The dimensions observed for YSZ and CeO_2 are in good agreement with the mean crystallite sizes calculated by XRD broadening (Table 2). Fig. 6 shows representative TEM images of the Ru- and Pd-based samples after activation by H_2 reduction at 150 °C. The morphology of both reduced catalysts is quite similar (Fig. 6a and b for Ru/CeO_2/YSZ and Pd/CeO_2/YSZ, respectively). Despite the prolonged thermal treatment at 750 °C applied on YSZ in order to stabilize its textural properties, the support grains present a rounded shape, with smoothed edged and corners. Although the surface area of the materials is not very high and the metal loading should be reasonable for a TEM investigation, the detection of metal nanoparticles was a hard task. This could be reasonably related with the low contrast between the metal phases (Ru or Pd) and the nanostructured support components (CeO_2 and YSZ) [64] or to the presence of a significant fraction of highly dispersed metal nanoparticles (as suggested by comparison of XRD and CO chemisorption data). TEM observations are local in nature. The metal nanoparticles could be located on specific places this suggesting it is difficult to exactly find them by TEM. Anyway, a number of metal nanoparticles were clearly identified on both the samples by TEM. Fig. 6c shows a representative Ru particle composed by two crystalline nanodomains with dimension of ~10 nm each while Fig. 6d presents a representative Pd nanoparticles of ~2 nm supported on a spherical CeO_2 particle deposited on YSZ, as confirmed by the measurements of the planar spacing and by the analysis of the morphology of the particles (Fig. 6).

After aging under ESR condition for 75 h at 550 °C, TEM images evidence some modifications on the morphology of the samples. (Fig. 7), In particular, carbon deposits with graphitic nature were identified from the lattice spacing (~0.351 nm) that are always in good agreement with the distance among graphite layers (d = 0.335 nm). The morphology of these deposits is very different in the two cases. On Ru/CeO_2/YSZ, carbon ribbons grow as filaments, in a similar way that previously observed for other metals, such as Ni [66,67]. This observation is in agreement with the good activity demonstrated by this catalyst and with the reduced but even accessible metal surface area. In fact, carbon filaments usually grow moving from one facet of a metal nanoparticle, leaving the remaining facets still available for adsorption of reagents. On the other hand, aged Pd/CeO_2/YSZ shows the presence of carbon deposits covering completely the surface of the metal particles. This result justifies the strong decrease of the accessible surface area evidenced in this sample. After a short catalytic period of time the Pd nanoparticles appear to package themselves in carbon this inhibiting subsequent catalytic activity.

3.2.6. *ThermoGravimetric Analysis (TGA)*

Fig. 8 shows the traces obtained by TGA analysis of the aged samples, performed in order estimate the amount of carbon deposits. A complex feature was obtained for both the samples. In both the cases, the weight changes are very limited, with an initial decrease of the weight followed by an increase above 500 °C. The final trend

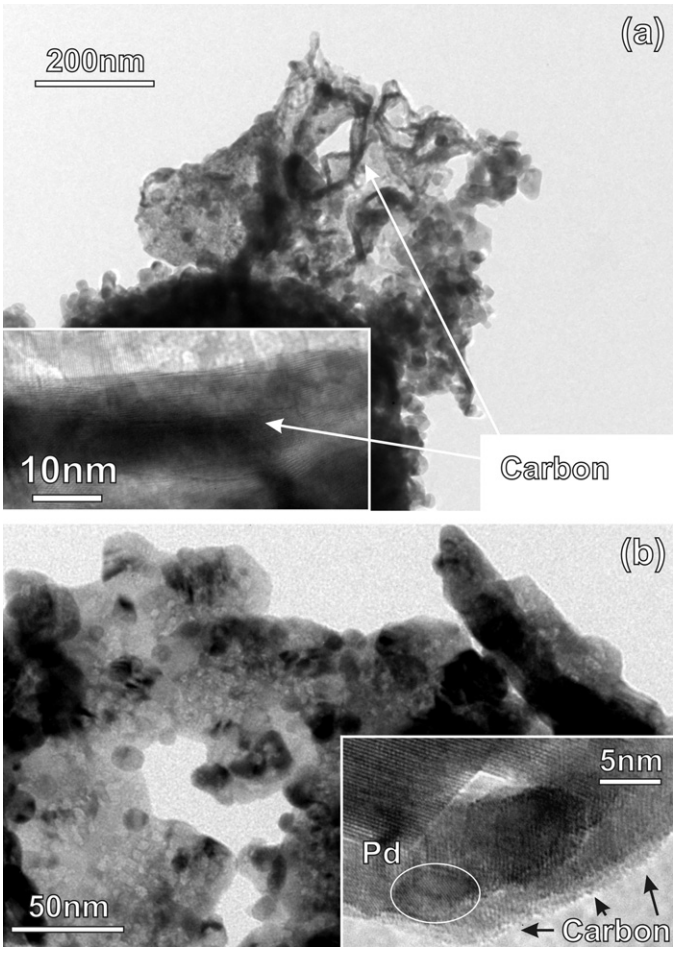

Fig. 7. Representative TEM images for the samples after aging under ESR conditions at 550 °C for 75 h: $Ru/CeO_2/YSZ$ (a) and $Pd/CeO_2/YSZ$ (b). Representative details of carbon deposits are shown in the insets.

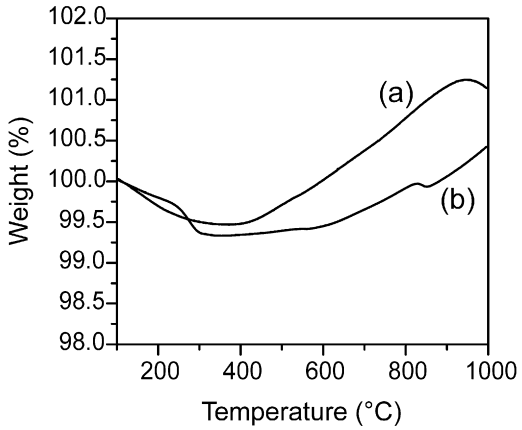

Fig. 8. ThermoGravimetric Analysis (TGA) of the samples after aging under ESR conditions for 75 h: $Ru/CeO_2/YSZ$ (a) and $Pd/CeO_2/YSZ$ (b).

in the weight of the materials is a combination of the loss due to carbon removal and of the gain due to reoxidation of reduced CeO_2 and metal nanoparticles. For both the materials, the first process predominates at low temperatures while the second becomes more important at higher temperatures. Considering that the amounts of O_2 acquired during the re-oxidation of the reduced materials is generally quite similar, the weight increase due to re-oxidation should be comparable. This result suggests that the amount of carbon residues deposited on the $Pd/CeO_2/YSZ$ is higher with respect to that present in the aged $Ru/CeO_2/YSZ$.

4. Conclusions

Ethanol steam reforming was investigated over $M/CeO_2/YSZ$ nanocomposites (M = Ru, Pd, Ag), as potential anodic components of SOFC. While Ru- and Pd-based systems showed promising activity, the silver containing catalyst presented very poor performances. Combination of TEM, Chemisorption and XRD data indicate that both Ru and Pd are subjected to partial metal sintering after prolonged high temperature aging. Small amount of coke is observed on both catalysts, the location and morphology of which strongly depends on the metal. Coke formation on $Pd/CeO_2/YSZ$ results in the occlusion of metal nanoparticles as amorphous layers, leading to a progressive and drastic deactivation of the catalyst. Less carbon is observed on Ru-based system and, more remarkably, it appears mostly as graphitic filaments. This latter form of coke allows a better accessibility of Ru with respect to the case of Pd. While total occlusion of the metal phase is an undesirable catalytic effect, the presence of a small amount of graphitic coke might positively increase the electronic conductivity of the anode of a SOFC, especially working at intermediate temperature [68].

Acknowledgements

Dr. M. Grzelczak and Prof. M. Prato (University of Trieste) are acknowledged for TGA measurements. University of Trieste, bilateral Italy-Argentina Project "Sustainable hydrogen production using noble metals supported on CeO_2-based nanocomposites", Fondo Trieste, PRIN2007 "2nd generation processes for the sustainable production of hydrogen" are acknowledged for the financial support.

References

[1] P. Barbaro, C. Bianchini, Catalysis for Sustainable Energy Production, 1st ed., Wiley–VCH, Weinheim, 2009.
[2] S. McIntosh, R.J. Gorte, Chem. Rev. 104 (2004) 4845–4865.
[3] M. Graziani, P. Fornasiero, Renewable Resources and Renewable Energy: A Global Challenge, 1st ed., Taylor & Francis, New York, 2007.
[4] S. Zinoviev, F. Muller-Langer, P. Das, N. Bertero, P. Fornasiero, M. Kaltschmitt, G. Centi, S. Miertus, ChemSusChem 3 (2010) 1106–1133.
[5] R.M. Navarro, M.A. Pena, J.L.G. Fierro, Chem. Rev. 107 (2007) 3952–3991.
[6] P.K. Cheekatamarla,.C.M. Finnerty, J. Power Sources 160 (2006) 490–499.
[7] V. Gombac, L. Sordelli, T. Montini, J.J. Delgado, A. Adamski, G. Adami, M. Cargnello, S. Bernal, P. Fornasiero, J. Phys. Chem. A 114 (2010) 3916–3925.
[8] B. Lorenzut, T. Montini, C.C. Pavel, M. Comotti, F. Vizza, C. Bianchini, P. Fornasiero, ChemCatChem 2 (2010) 1096–1196.
[9] M. Galbe, G. Zacchi, Appl. Microbiol. Biotechnol. 59 (2002) 618–628.
[10] B.S. Dien, M.A. Cotta, T.W. Jeffries, Appl. Microbiol. Biotechnol. 63 (2003) 258–266.
[11] J. Kugai, S. Velu, C.S. Song, Catal. Lett. 101 (2005) 255–264.
[12] J. Rasko, A. Hancz, A. Erdohelyi, Appl. Catal. A: Gen. 269 (2004) 13–25.
[13] A.N. Fatsikostas, D.I. Kondarides, X.E. Verykios, Chem. Commun. (2001) 851–852.
[14] M.C. Sanchez-Sanchez, R.M. Navarro, J.L.G. Fierro, Int. J. Hydrogen Energ. 32 (2007) 1462–1471.
[15] M. Ni, D.Y.C. Leung, M.K.H. Leung, Int. J. Hydrogen Energ. 32 (2007) 3238–3247.
[16] T. Montini, L. De Rogatis, V. Gombac, P. Fornasiero, M. Graziani, Appl. Catal. B: Environ. 71 (2007) 125–134.
[17] D.K. Liguras, D.I. Kondarides, X.E. Verykios, Appl. Catal. B: Environ. 43 (2003) 345–354.
[18] S. Bernal, J.J. Calvino, M.A. Cauqui, J.A.P. Omil, J.M. Pintado, J.M. Rodriguez-Izquierdo, Appl. Catal. B: Environ. 16 (1998) 127–138.
[19] G. Vlaic, P. Fornasiero, G. Martra, E. Fonda, J. Kaspar, L. Marchese, E. Tomat, S. Coluccia, M. Graziani, J. Catal. 190 (2000) 182–190.
[20] P. Fornasiero, G. Balducci, R. DiMonte, J. Kaspar, V. Sergo, G. Gubitosa, A. Ferrero, M. Graziani, J. Catal. 164 (1996) 173–183.
[21] G. Colon, M. Pijolat, F. Valdivieso, H. Vidal, J. Kaspar, E. Finocchio, M. Daturi, C. Binet, J.C. Lavalley, R.T. Baker, S. Bernal, J. Chem. Soc. Faraday Trans. 94 (1998) 3717–3726.
[22] J. Kaspar, P. Fornasiero, M. Graziani, Catal. Today 50 (1999) 285–298.
[23] S. Adhikari, S.D. Fernando, S.D.F. To, R.M. Bricka, P.H. Steele, A. Haryanto, Energ. Fuels 22 (2008) 1220–1226.

[24] D.V. Andreev, S.V. Korotaev, R.M. Khantakov, L.L. Makarshin, A.G. Gribovskii, L.P. Davydova, V.N. Parmon, Kinet. Catal. 50 (2009) 241–246.
[25] X. Cai, Y. Cai, W. Lin, J. Nat. Gas Chem. 17 (2008) 201–207.
[26] S. Corthals, J. Van Nederkassel, J. Geboers, H. De Winne, J. Van Noyen, B. Moens, B. Sels, P. Jacobs, Catal. Today 138 (2008) 28–32.
[27] A.P. Ferreira, D. Zanchet, J.C.S. Arajo, J.W.C. Liberatori, E.F. Souza-Aguiar, F.B. Noronha, J.M.C. Bueno, J. Catal. 263 (2009) 335–344.
[28] C.L. Li, Y.L. Fu, G.Z. Bian, Chin. J. Catal. 24 (2003) 187–192.
[29] Y. Liu, T. Hayakawa, T. Tsunoda, K. Suzuki, S. Hamakawa, K. Murata, R. Shiozaki, T. Ishii, M. Kumagai, Top. Catal. 22 (2003) 205–213.
[30] A. Nandini, K.K. Pant, S.C. Dhingra, Appl. Catal. A: Gen. 308 (2006) 119–127.
[31] C.W. Sun, Z. Xie, C.R. Xia, H. Li, L.Q. Chen, Electrochem. Commun. 8 (2006) 833–838.
[32] O. Görke, P. Pfeifer, K. Schubert, Appl. Catal. A: Gen. 360 (2009) 232–241.
[33] P. Djinovi-ç, J. Batista, J. Levec, A. Pintar, Appl. Catal. A: Gen. 364 (2009) 156–165.
[34] M.M. Mohamed, T.M. Salama, A.I. Othman, G.A. El Shobaky, Appl. Catal. A: Gen. 279 (2005) 23–33.
[35] M. Manzoli, G. Avgouropoulos, T. Tabakova, J. Papavasiliou, T. Ioannides, F. Boccuzzi, Catal. Today 138 (2008) 239–243.
[36] O. Pozdnyakova-Tellinger, D. Teschner, J. hnert, F.C. Jentoft, A. Knop-Gericke, R. gl, A. Wootsch, J. Phys. Chem. C 111 (2007) 5426–5431.
[37] J.W. Fergus, J. Power Sources 162 (2006) 30–40.
[38] K.Y. Ahn, H.P. He, J.M. Vohs, R.J. Gorte, Electrochem. Solid State 8 (2005) A414–A417.
[39] C. Lu, W.L. Worrell, R.J. Gorte, J.M. Vohs, J. Electrochem. Soc. 150 (2003) A354–A358.
[40] A. Hornés, D. Gamarra, G. Munuera, J.C. Conesa, A. Martinez-Arias, J. Power Sources 169 (2007) 9–16.
[41] M.D. Gross, J.M. Vohs, R.J. Gorte, J. Electrochem. Soc. 154 (2007) 694–699.
[42] S.W. Jung, C. Lu, H.P. He, K.Y. Ahn, R.J. Gorte, J.M. Vohs, J. Power Sources 154 (2006) 42–50.
[43] T. Kim, G. Liu, M. Boaro, S.I. Lee, J.M. Vohs, R.J. Gorte, O.H. Al Madhi, B.O. Dabbousi, J. Power Sources 155 (2006) 231–238.
[44] M. Cimenti,.J.M. Hill, Asia–Pac. J. Chem. Eng. 4 (2009) 45–54.
[45] M. Cimenti,.J.M. Hill, J. Power Sources 195 (2010) 3996–4001.
[46] T. Nishiguchi, T. Matsumoto, H. Kanai, K. Utani, Y. Matsumura, W.J. Shen, S. Imamura, Appl. Catal. A: Gen. 279 (2005) 273–277.
[47] E. Vesselli, G. Comelli, R. Rosei, S. Freni, F. Frusteri, S. Cavallaro, Appl. Catal. A: Gen. (2005) 139–147.
[48] E. Vesselli, A. Baraldi, G. Comelli, S. Lizzit, R. Rosei, ChemPhysChem 5 (2004) 1133–1140.
[49] F. Melo, N. Morlanés, Catal. Today 133–135 (2008) 374–382.
[50] H.J. Lee, Y.S. Lim, N.C. Park, Y.C. Kim, Chem. Eng. J. 146 (2009) 295–301.
[51] F. Basile, L. Basini, G. Fornasari, M. Gazzano, F. Trifiro, A. Vaccari, Chem. Commun. (1996) 2435–2436.
[52] V. Sadykov, N. Mezentseva, G. Alikina, R. Bunina, V. Pelipenko, A. Lukashevich, S. Tikhov, V. Usoltsev, Z. Vostrikov, O. Bobrenok, A. Smirnova, J. Ross, O. Smorygo, B. Rietveld, Catal. Today 146 (2009) 132–140.
[53] Y. Shen, S. Wang, C. Luo, H. Liu, Prog. Chem. 19 (2007) 431–436.
[54] A.L. Sauvet,.J. Fouletier, J. Power Sources 101 (2001) 259–266.
[55] V. Choque, P.R. de la Piscina, D. Molyneux, N. Homs, Catal. Today 149 (2010) 248–253.
[56] S. Rabe, T.B. Truong, F. Vogel, Appl. Catal. A: Gen. 292 (2005) 177–188.
[57] J.J. Carroll, K.L. Haug, J.C. Weisshaar, M.R.A. Blomberg, P.E.M. Siegbahn, M. Svensson, J. Phys. Chem. 99 (1995) 13955–13969.
[58] R. Di Monte, P. Fornasiero, J. Kaspar, M. Graziani, J.M. Gatica, S. Bernal, A. Gomez-Herrero, Chem. Commun. (2000) 2167–2168.
[59] G. Kim, J.M. Vohs, R.J. Gorte, J. Mater. Chem. 18 (2008) 2386–2390.
[60] P. Fornasiero, R. DiMonte, G.R. Rao, J. Kaspar, S. Meriani, A. Trovarelli, M. Graziani, J. Catal. 151 (1995) 168–177.
[61] A. Trovarelli, G. Dolcetti, C. de Leitenburg, J. Kaspar, Stud. Surf. Sci. Catal. 75 (1993) 2781–2784.
[62] E.S. Putna, T. Bunluesin, X.L. Fan, R.J. Gorte, J.M. Vohs, R.E. Lakis, T. Egami, Catal. Today 50 (1999) 343–352.
[63] S. Bernal, J.J. Calvino, G.A. Cifredo, A. Laachir, V. Perrichon, J.M. Herrmann, Langmuir 10 (1994) 717–722.
[64] J.M. Gatica, R.T. Baker, P. Fornasiero, S. Bernal, J. Kaspar, J. Phys. Chem. B 105 (2001) 1191–1199.
[65] J.M. Gatica, R.T. Baker, P. Fornasiero, S. Bernal, G. Blanco, J. Kaspar, J. Phys. Chem. B 104 (2000) 4667–4672.
[66] M. Ito, T. Tagawa, S. Goto, J. Chem. Eng. Jpn. 32 (1999) 274–279.
[67] J.B. Wang, Y.S. Wu, T.J. Huang, Appl. Catal. A: Gen. 272 (2004) 289–298.
[68] H.P. He, J.M. Vohs, R.J. Gorte, J. Power Sources 144 (2005) 135–140.